Observation of intrinsic chiral bound states in the continuum

https://doi.org/10.1038/s41586-022-05467-6

Received: 6 May 2022

Accepted: 20 October 2022

Published online: 18 January 2023

Check for updates

Yang Chen[1,2,6], Huachun Deng[3,6], Xinbo Sha[3,6], Weijin Chen[2,6], Ruize Wang[1], Yu-Hang Chen[1], Dong Wu[1], Jiaru Chu[1], Yuri S. Kivshar[4], Shumin Xiao[3,5]✉ & Cheng-Wei Qiu[2]✉

Photons with spin angular momentum possess intrinsic chirality, which underpins many phenomena including nonlinear optics[1], quantum optics[2], topological photonics[3] and chiroptics[4]. Intrinsic chirality is weak in natural materials, and recent theoretical proposals[5–7] aimed to enlarge circular dichroism by resonant metasurfaces supporting bound states in the continuum that enhance substantially chiral light–matter interactions. Those insightful works resort to three-dimensional sophisticated geometries, which are too challenging to be realized for optical frequencies[8]. Therefore, most of the experimental attempts[9–11] showing strong circular dichroism rely on false/extrinsic chirality by using either oblique incidence[9,10] or structural anisotropy[11]. Here we report on the experimental realization of true/intrinsic chiral response with resonant metasurfaces in which the engineered slant geometry breaks both in-plane and out-of-plane symmetries. Our result marks, to our knowledge, the first observation of intrinsic chiral bound states in the continuum with near-unity circular dichroism of 0.93 and a high quality factor exceeding 2,663 for visible frequencies. Our chiral metasurfaces may lead to a plethora of applications in chiral light sources and detectors, chiral sensing, valleytronics and asymmetric photocatalysis.

Chirality, a fundamental trait of nature, refers to the geometric attribute of objects that lack mirror-reflection symmetry. To evaluate how chiral an object is, electromagnetic chirality, with the manifestation of circular dichroism (CD), is conventionally adopted based on the differential interactions between the object and electromagnetic fields of different handedness[12,13]. However, it is found that planar structures with out-of-plane mirror symmetry, which are not supposed to be chiral, can still demonstrate strong CD signals through the introduction of structural anisotropy[14] or oblique incidence[15,16]. In these cases, the amplitude of CD cannot measure the 'true chirality' or 'intrinsic chirality' of an object, but it is originated from anisotropy-induced polarization conversion or chiral configurations of the experimental setup, which are usually called 'false chirality' or 'extrinsic chirality'[15–18]. Although false chirality may yield similar CD signals as its counterpart of true chirality, its applications in a range of important fields such as chiral emission and polarized photodetection are notably limited.

Apart from intrinsic chirality, another key parameter for enhancing the strength of chiral light–matter interactions is the quality (Q) factor of the associated resonance. Owing to the potential applications in chiral emission, chiral sensing and enantiomer separation, high-Q resonances with large intrinsic chirality have long been pursued but remain unexplored. Chiral metamaterials and metasurfaces can produce strong chiroptical responses[19–21], but their achieved Q-factors are still low, typically less than 200, owing to large radiative and non-radiative losses.

Recently, the physics of bound states in the continuum (BICs) has been used in photonics to achieve and engineer high-Q resonances[22–25]. When a BIC acquires intrinsic chirality, the resulting chiral BIC can simultaneously generate high Q-factors and strong CDs without involving extrinsic chirality. As pointed out by previous theoretical works, the key to enabling the chiral BIC is to break all the mirror symmetries of the structure[5–7], which has hindered its experimental realization. We have witnessed numerous approaches that break either the in-plane[24,26] or the out-of-plane[27] mirror symmetry, but the remaining symmetry planes still prevent the generation of intrinsic chiral BICs. The measured high-Q CD resonances are inevitably attributed to the false chirality of oblique incidence[9,10] or polarization conversion[11].

Here we report the optical realization of intrinsic chiral BICs based on a new paradigm of slant-perturbation metasurfaces. The metasurface is composed of a square array of slanted trapezoid nanoholes in a TiO_2 film, which is placed on a glass substrate and covered with PMMA (Fig. 1a). This structure is evolved from vertical square nanoholes by introducing two types of perturbations, an in-plane deformation angle α and an out-of-plane slant angle φ, so that all the mirror symmetries are broken. A series of Bloch modes are supported by the metasurface (Fig. 1b), the mode profiles of which are shown in Supplementary Fig. 1. Without loss of generality, we first consider the fundamental transverse magnetic (TM_1) mode. When no perturbations are involved ($\alpha = 0$, $\varphi = 0$), it supports a symmetry-protected BIC at the Γ point of the

[1]Chinese Academy of Sciences Key Laboratory of Mechanical Behavior and Design of Materials, Department of Precision Machinery and Precision Instrumentation, University of Science and Technology of China, Hefei, China. [2]Department of Electrical and Computer Engineering, National University of Singapore, Singapore, Singapore. [3]Ministry of Industry and Information Technology Key Lab of Micro-Nano Optoelectronic Information System, Harbin Institute of Technology, Shenzhen, P. R. China. [4]Nonlinear Physics Center, Research School of Physics, Australian National University, Canberra, New South Wales, Australia. [5]Pengcheng Laboratory, Shenzhen, P. R. China. [6]These authors contributed equally: Yang Chen, Huachun Deng, Xinbo Sha, Weijin Chen. ✉e-mail: shumin.xiao@hit.edu.cn; chengwei.qiu@nus.edu.sg

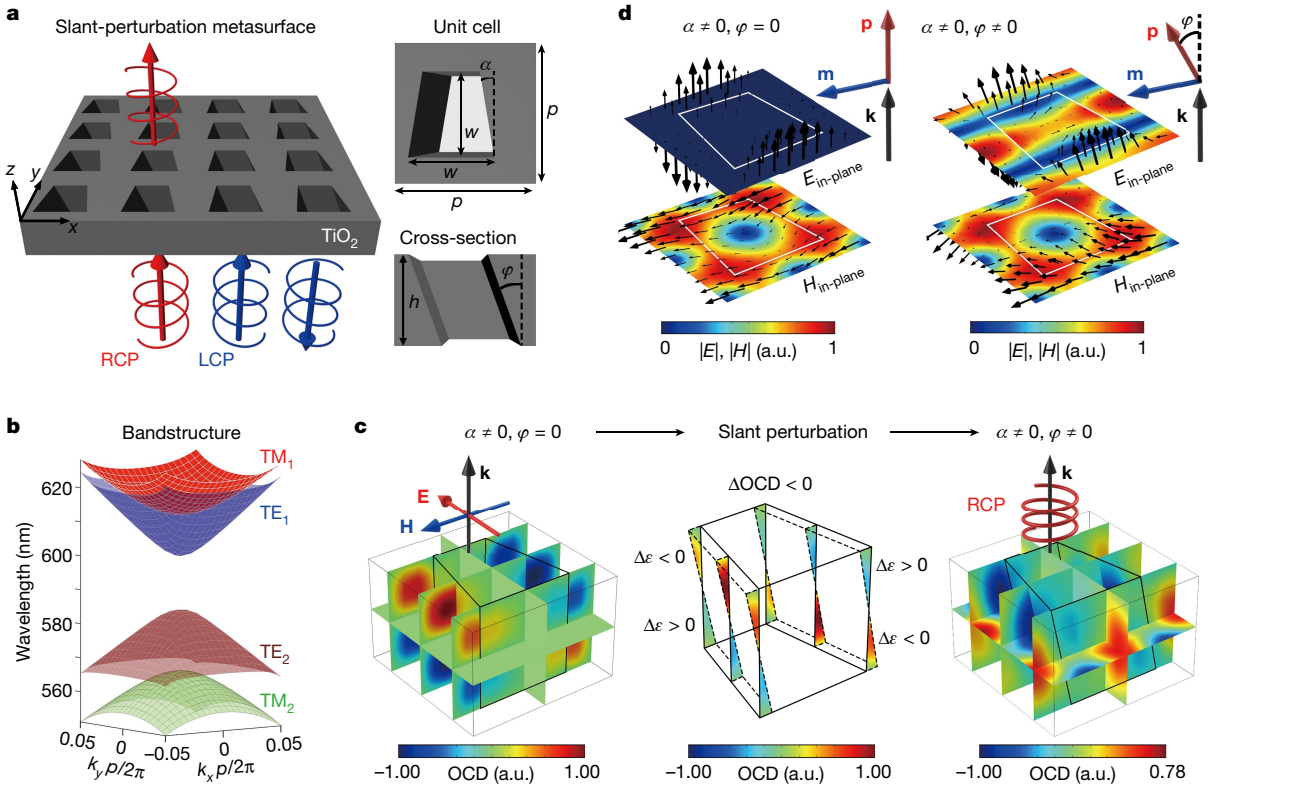

Fig. 1 | Origin of intrinsic chirality induced by slant perturbation. **a**, Schematic of the slant-perturbation metasurface to realize intrinsic chiral BICs. The geometric parameters are: $p = 340$ nm, $w = 210$ nm, $h = 220$ nm. **b**, Calculated bandstructure of the metasurface with only non-degenerate modes plotted. **c**, Cross-sectional OCD distributions for the case of $\alpha \neq 0, \varphi = 0$ (left) and $\alpha \neq 0, \varphi \neq 0$ (right). OCD distributions in the slant-perturbed areas are highlighted in the middle panel with their permittivity change ($\Delta\varepsilon$) indicated. **d**, In-plane components of electric ($E_{\text{in-plane}}$) and magnetic ($H_{\text{in-plane}}$) field distributions at the central x–y plane of the metasurface without (left) and with (right) slant perturbation, along with the configurations of the corresponding electric dipole $\boldsymbol{p}$ and magnetic dipole $\boldsymbol{m}$.

Brillouin Zone because of the C_2^z symmetry of the structure. Owing to time-reversal symmetry, the electromagnetic near fields are always linearly polarized for BICs and their distributions cancel each other to stop far-field radiation (Supplementary Information Section 2).

Once an in-plane geometric perturbation is introduced to break the C_2^z symmetry, for example, the square nanohole is cut into a trapezoid ($\alpha \neq 0, \varphi = 0$), the BIC evolves to a quasi-BIC possessing circular polarizations in the near field, the chirality of which can be evaluated by the optical chirality density[28,29]: $\mathrm{OCD} = (-\frac{1}{2})\omega \mathrm{Re}[\mathbf{D}\bullet\mathbf{B}^*]$, where ω is the angular frequency of light, $\mathbf{D}$ is the electric displacement field, and $\mathbf{B}^*$ is the complex conjugation of magnetic flux density. Because the optical chirality density (OCD) is a parity-odd scalar[30], the existence of a mirror symmetry forces it to have opposite values on the two sides of the mirror as shown in Fig. 1c. In the far field, the Stokes parameter S_3 of the radiation is related to the optical chirality flux $\mathcal{F}$ by the equation $S_3 = \frac{c}{\omega \mathcal{S}} \int_V \mathrm{Re}(\nabla\bullet\mathcal{F})\,\mathrm{d}v$, where $\mathcal{S}$ is the power flux, c is the light velocity, V is a finite volume including the slab and the surrounding background zone, $\mathrm{d}v$ is the volume element and $\mathcal{F}$ is defined as $\mathcal{F} = \frac{1}{4}[\mathbf{E} \times (\nabla \times \mathbf{H}^*) - \mathbf{H}^* \times (\nabla \times \mathbf{E})]$. In analogy to Poynting's theorem, optical chirality is also bounded by the conservation law. Thus, the optical chirality flux $\mathcal{F}$ is directly related to the near-field OCD of the associated resonance by the equation

$$-2\omega \int_V \mathrm{OCD}\,\mathrm{d}v + \int_V \mathrm{Re}(\nabla\bullet\mathcal{F})\,\mathrm{d}v = 0 \qquad (1)$$

Here the antisymmetric OCD distributions cancel each other in the near field of the metasurface and, hence, generate no chiral flux in the far field. The absence of far-field chiral flux is protected by out-of-plane mirror symmetry and is immune from in-plane geometries.

One of the most convenient methods to break the out-of-plane mirror symmetry is to slant the nanohole in the x direction. Then the variation of OCD is written as $\Delta\mathrm{OCD} = (\Delta\varepsilon/\varepsilon) \times \mathrm{OCD}$, where $(\Delta\varepsilon/\varepsilon)$ denotes the change of permittivity divided by its original value. As highlighted in Fig. 1c (middle panel), $\Delta\varepsilon$ and OCD have opposite signs in all perturbed areas and hence the volume-integrated ΔOCD is negative. The unbalanced OCD distributions in the near field of the slant-perturbation metasurface will induce non-zero optical chirality flux in the far field, corresponding to circularly polarized radiation (Fig. 1c).

The origin of slant-induced chirality can also be analysed by examining the near-field electromagnetic distributions at the central x–y plane. As shown in Fig. 1d, when no slant perturbation is introduced, the magnetic fields of quasi-BICs are predominantly x polarized whereas the electric fields are out-of-plane. According to the generalized theory of chiroptics[12,15], the optical chirality of an object in the dipole approximation is controlled by the dot product $\mathbf{p}_\perp \cdot \mathbf{m}_\perp$, where $\mathbf{p}_\perp$ and $\mathbf{m}_\perp$ are the projections of the associated electric dipole $\mathbf{p}$ and magnetic dipole $\mathbf{m}$ on the plane perpendicular to the $\mathbf{k}$ vector of incident light. Here $\mathbf{p}$ is parallel to $\mathbf{k}$, resulting in no optical chirality. To break such a parallel configuration, the nanohole can be slanted towards the negative x direction so that the associated electric field vectors are tilted towards the same direction, while the magnetic fields approximately remain x polarized (Fig. 1d), leading to non-zero $\mathbf{p}_\perp \cdot \mathbf{m}_\perp$ and optical chirality.

In Fig. 2a, we calculate the unbalanced OCD that is equal to $\int_V \mathrm{OCD}\,\mathrm{d}v$ as a function of the slant angle for different quasi-BICs. It can now be seen that an optimal slant angle exists for attaining the maximal unbalanced OCD in which the largest degree of circular polarization of far-field radiation is anticipated. We can also see that the amplitude of unbalanced OCD cannot reach unity through the slant operation alone

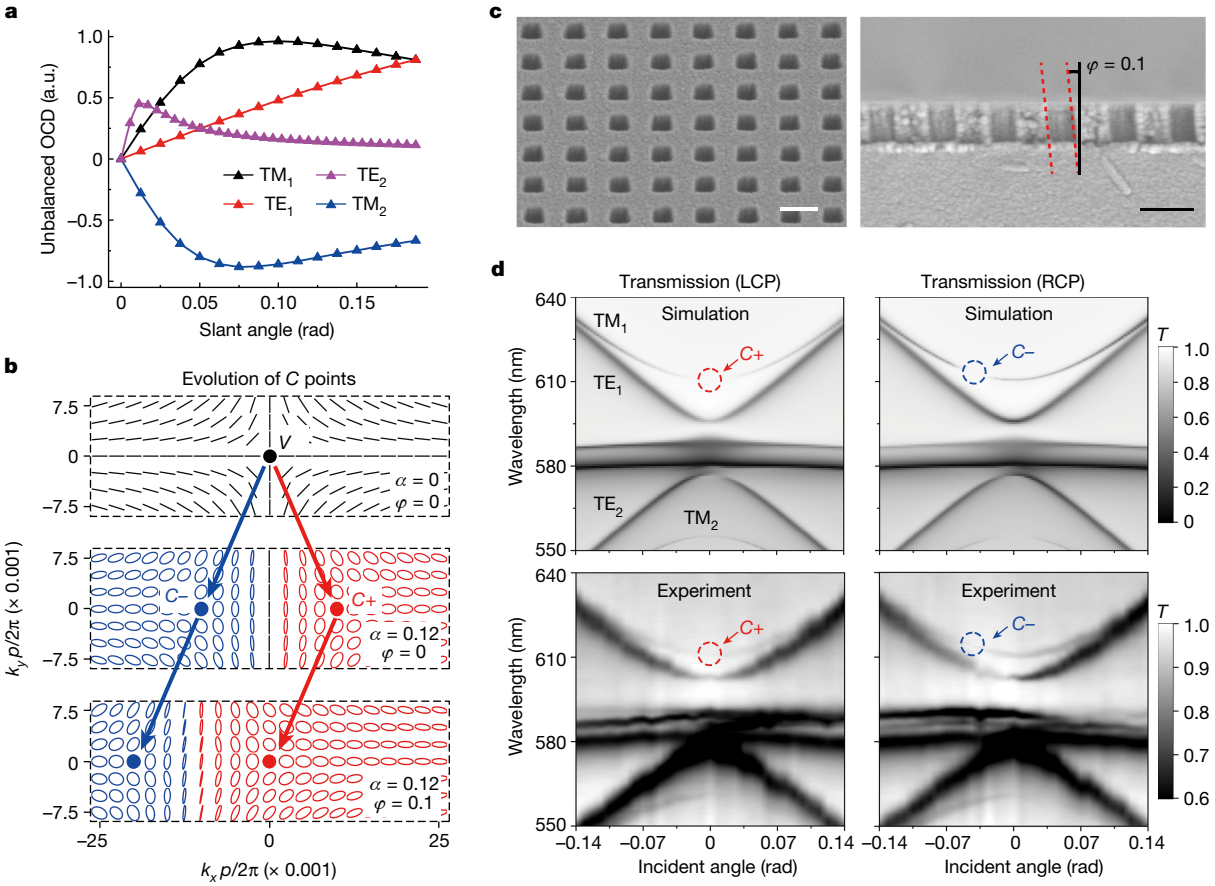

Fig. 2 | Design, fabrication and characterization of slant-perturbation metasurfaces. a, Unbalanced OCD integrated over the metasurface as a function of the slant angle for different quasi-BICs. **b**, Evolution of *C* points over *k*-space for the metasurfaces of different α and φ. The elliptical polarizations are represented by ellipses of red or blue colours corresponding to right- or left-handed states, whereas the black lines represent linear polarizations. **c**, Side-view (left) and cross-sectional (right) scanning electron microscope images of a fabricated metasurface. Scale bar, 300 nm. **d**, Angle-resolved transmission spectra of the metasurface under LCP (left) and RCP (right) incidence obtained from simulations (top) and experiments (bottom). **d**, Incident angles at which *C*+ and *C*− points are observed for different slant angles φ, retrieved from simulations and experiments.

for the second-order transverse magnetic (TM_2) and transverse electric (TE_2) modes. For the fundamental transverse electric (TE_1) mode, the slant angle needs to be larger to obtain large unbalanced OCD, and inevitably leads to a much smaller *Q*-factor. Thus, the TM_1 mode is found to be the best candidate for achieving intrinsic chiral BICs with large *Q*-factor.

The evolution of the momentum-space eigenpolarization map of TM_1 along with geometric perturbations is presented in Fig. 2b. For the unperturbed case, BIC is manifested by an at-Γ *V* point in the map to represent a polarization singularity. Once a non-zero α is induced, the integer-charged *V* point is decomposed into a pair of half-charged *C* points distributed symmetrically on the two sides of the Γ point, where the *C*+ and *C*− points possess right-handed circular polarization (RCP) and left-handed circular polarization (LCP), respectively. Further, if a non-zero φ is introduced as well, the polarization map as a whole is moved in the same direction of structural inclination. For a proper combination of α and φ, for example, $\alpha = 0.12$ and $\varphi = 0.1$, the *C*− point is shifted further to the left, while the *C*+ point can be located right at the Γ point, leading to the achievement of an intrinsic chiral BIC (Fig. 2b). Similarly, we can also create chiral BIC in the TE_1 mode (Supplementary Fig. 3). The role played by the index-matched PMMA layer is discussed in Supplementary Information Section 4.

The proposed metasurface is fabricated by a modified slanted-etching system (see details in the Methods and Supplementary Fig. 5). For the accurate control of small slant angles, the sample is placed on a wedged substrate and an Al_2O_3 screen with an aperture is laid above the sample acting as an ion collimator. The scanning electron microscope images of fabricated samples are shown in Fig. 2c and Supplementary Fig. 6. Because of the usage of an ion collimator, the left and right sidewalls exhibit an almost identical slant angle. The angle-resolved transmission spectra of a slant-perturbation metasurface ($\alpha = 0.12$, $\varphi = 0.1$) under RCP and LCP incidence are simulated in Fig. 2d. It is observed that the *C*+ point represented by the diminishing point in the TM_1 band of LCP incidence appears at a normal direction, that is, the Γ point. However, for the RCP incidence case, the TM_1 mode can be excited at normal incidence, and the *C*− point is observed at the incidence angle of −0.04 rad. The experimental results agree well with simulations, in which the measured *C*+ and *C*− points are present at the incidence angles of 0 and −0.044 rad, respectively (Fig. 2d). The details of the optical experimental setup are provided in the Methods and Supplementary Fig. 7.

To study the evolution of *C* points with the slant angle, we have fabricated a series of metasurfaces with a fixed α but variable φ. As retrieved from transmission spectra, the incident angles at which *C*+ and *C*− points occur approximately follow linear relationships with φ, which is consistent with the simulation results (Fig. 3a). Apparently, the key point for achieving chiral BICs is to cooperatively modulate α and φ, so that one *C* point is generated and then moved back to the Γ point. To reveal such an inherent linkage between α and φ, the generalized model based on electric and magnetic dipoles shown in Fig. 1d is revisited. When the associated perturbations α and φ are small, the *Q*-factor of quasi-BICs roughly scales with the inversely quadratic square of all

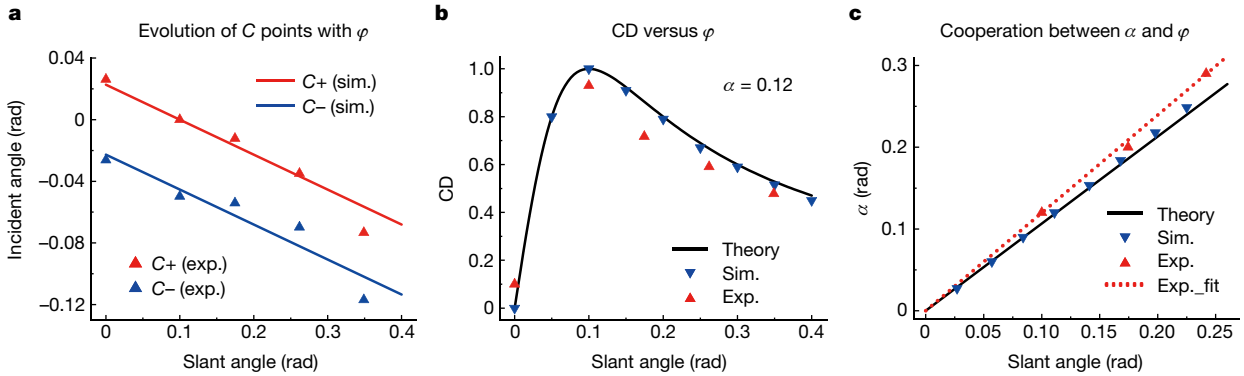

Fig. 3 | Inherent linkage between geometric perturbations for achieving chiral BICs. a, Incident angles for which *C*+ and *C*− points are observed for different slant angles φ, retrieved from simulations and experiments. **b**, CD amplitude as a function of φ while α is fixed at 0.12. Theoretical, simulation (sim.) and experimental (exp.) results are included for comparison. **c**, Relation between φ and α for maximizing CD. The experimental data points are fitted by a linear relation (Exp._fit).

the perturbations[24]: $Q \sim 1/(\alpha^2 + A\varphi^2)$, where A expresses the different sensitivities of Q to α and φ. Meanwhile, the amplitudes of the electric dipole **p** and magnetic dipole **m** are proportional to the square root of the Q-factor: $|\mathbf{p}| \sim Q^{1/2}$ and $|\mathbf{m}| \sim Q^{1/2}$. Then, the intrinsic chirality of quasi-BICs, manifested by CD, can be estimated by:

$$\mathrm{CD} \sim \mathbf{p}_{\perp} \cdot \mathbf{m}_{\perp} = |\mathbf{p}|\,|\mathbf{m}|\,\sin(\varphi) \sim \frac{\sin(\varphi)}{\alpha^2 + A\varphi^2} \approx \frac{\varphi}{\alpha^2 + A\varphi^2} \qquad (2)$$

As predicted by equation (2), if φ is raised from zero while α is fixed, CD will first rapidly increase to the maximum and then gradually decrease. This is well reproduced by the results of simulations (Fig. 3b). The experimental results also follow a similar dependence, except that the measured CDs are smaller than the simulated ones (see detailed spectral data in Supplementary Fig. 8). Such a deviation is mainly attributed to the fabrication tolerance and the undesired scattering from surface roughness. Further, by calculating the derivative of CD versus φ, the condition for maximizing CD is deduced to be $\alpha = \sqrt{A} \times \varphi$. This offers a straightforward recipe to select a suitable set of φ and α for achieving chiral BICs. The slope $\sqrt{A}$ is related to the mode profile and could take different values for different chiral BICs. For the TM_1 mode, the slope is theoretically predicted to be 1.066 (Supplementary Information Section 8), which agrees well with the simulation results (Fig. 3c). The experimental data also follow a linear relationship and the fitted slope of 1.197 slightly deviates from the predicted one. Accordingly, as long as φ and α are cooperatively decreased, the Q-factor of chiral BICs can be continuously boosted while maintaining a CD of unity (Supplementary Information Section 9). In our experiments, φ and α are set as 0.1 and 0.12, respectively, owing to the fabrication capacity. We notice that the slant direction of the nanohole can also be rotated with an azimuthal angle θ, the impact of which is discussed in Supplementary Information Section 10.

Another way to raise the Q-factor of chiral BICs is to enlarge the metasurface size, so that both in-plane and out-of-plane leakage are suppressed[31]. We have fabricated a group of metasurface samples with different sizes. The highest Q-factor of 2,663 is obtained for the largest sample of 200 μm and the maximum CD is also reached, with a value of 0.93 (Fig. 4a). Here CD is defined as $\mathrm{CD} = (R_R - R_L)/(R_R + R_L)$, where $R_{R(L)}$ is the normalized reflection spectra under RCP (LCP) illumination. The near-field distributions under RCP and LCP illuminations are presented in Supplementary Fig. 12. To exclude the possible impact of structural anisotropy, we have measured the normalized reflection matrix $R = [R_{RR}, R_{RL}; R_{LR}, R_{LL}]$ on a circular basis, where the notation R_{RL} refers to the reflection of RCP light under LCP incidence. As shown in Fig. 4b, the cross-polarized components, R_{RL} and R_{LR}, possess negligible intensities, suggesting the absence of polarization conversion. It is thus concluded that the observed CD signal is attributed to the intrinsic chirality of quasi-BICs. The measured transmission spectra are included in Supplementary Fig. 13. The fundamental difference between our demonstrated intrinsic chiral BICs and other BIC works relying on extrinsic chirality to generate large CDs is explicitly discussed in Supplementary Information Section 13.

In Fig. 4c, we have summarized the experimental Q-factors and CDs from some typical works about chiral metamaterials and/or metasurfaces[11,14,32–40]. These works are divided into two categories according to the origin of the CD signals: one purely relies on the intrinsic chirality of

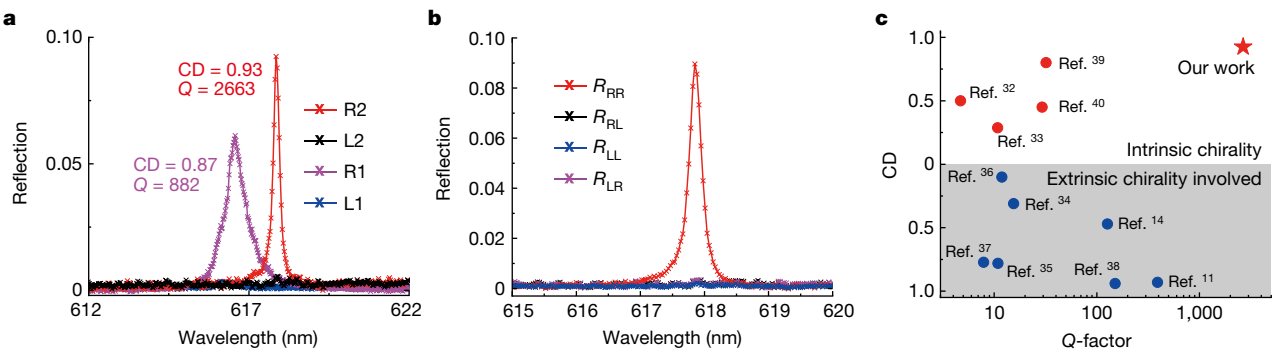

Fig. 4 | Giant CD and *Q*-factor enabled by intrinsic chiral BICs. a, Measured reflection spectra of the two metasurface samples of 68 μm (L1 and R1) and 200 μm sizes (L2 and R2) under LCP and RCP incidence, respectively. Their retrieved CDs and Q-factors are marked. **b**, Measured reflection matrix R in the circular basis for the 200 μm sample. **c**, CDs and Q-factors obtained from some typical experimental works as compared to our work. They are classified into two categories: intrinsic chirality and extrinsic chirality involved, according to the origin of the CD signals.

associated resonance and the other also has extrinsic chirality involved. Clearly, most approaches achieving high CDs rely on extrinsic chirality effects[11,35,37,38] and their Q-factors are still much smaller than ours. It is noted that the previous works exhibiting relatively large Q-factors are inevitably conducted in the infrared spectra[11,38,39], highlighting the great difficulty and significance of achieving intrinsic chiral BICs in the visible spectrum.

In conclusion, we have presented, to our knowledge, the first experimental observation of optical chiral BICs enabling simultaneously high values of the Q-factor (Q = 2663) and a near-unity CD of 0.93. We have developed a microscopic model based on the variation of local spin density to explain the origin of optical chirality. Although our chiral BIC metasurface is demonstrated in the visible spectrum, the concept is general, being applicable to the infrared and longer spectra and promising future applications for chiral light sources and detectors, chiral sensing, quantum optics and asymmetric photocatalysis.

Online content

Any methods, additional references, Nature Portfolio reporting summaries, source data, extended data, supplementary information, acknowledgements, peer review information; details of author contributions and competing interests; and statements of data and code availability are available at https://doi.org/10.1038/s41586-022-05467-6.

1. Collins, J. T. et al. First observation of optical activity in hyper-Rayleigh scattering. *Phys. Rev. X* **9**, 011024 (2019).
2. Lodahl, P. et al. Chiral quantum optics. *Nature* **541**, 473–480 (2017).
3. Parappurath, N., Alpeggiani, F., Kuipers, L. & Verhagen, E. Direct observation of topological edge states in silicon photonic crystals: spin, dispersion, and chiral routing. *Sci. Adv.* **6**, eaaw4137 (2020).
4. Chen, Y. et al. Multidimensional nanoscopic chiroptics. *Nat. Rev. Phys.* **4**, 113–124 (2021).
5. Gorkunov, M. V., Antonov, A. A. & Kivshar, Y. S. Metasurfaces with maximum chirality empowered by bound states in the continuum. *Phys. Rev. Lett.* **125**, 093903 (2020).
6. Overvig, A., Yu, N. & Alu, A. Chiral quasi-ound states in the continuum. *Phys. Rev. Lett.* **126**, 073001 (2021).
7. Dixon, J., Lawrence, M., Barton, D. R. & Dionne, J. Self-isolated raman lasing with a chiral dielectric metasurface. *Phys. Rev. Lett.* **126**, 123201 (2021).
8. Gorkunov, M. V., Antonov, A. A., Tuz, V. R., Kupriianov, A. S. & Kivshar, Y. S. Bound states in the continuum underpin near-lossless maximum chirality in dielectric metasurfaces. *Adv. Opt. Mater.* **9**, 2100797 (2021).
9. Liu, W. et al. Circularly polarized states spawning from bound states in the continuum. *Phys. Rev. Lett.* **123**, 116104 (2019).
10. Wu, J. et al. Observation of giant extrinsic chirality empowered by quasi-bound states in the continuum. *Phys. Rev. Appl.* **16**, 064018 (2021).
11. Shi, T. et al. Planar chiral metasurfaces with maximal and tunable chiroptical response driven by bound states in the continuum. *Nat. Commun.* **13**, 4111 (2022).
12. Barron, L. D. *Molecular Light Scattering and Optical Activity* (Cambridge Univ. Press, 2004).
13. Fernandez-Corbaton, I., Fruhnert, M. & Rockstuhl, C. Objects of maximum electromagnetic chirality. *Phys. Rev. X* **6**, 031013 (2016).
14. Wu, C. et al. Spectrally selective chiral silicon metasurfaces based on infrared Fano resonances. *Nat. Commun.* **5**, 3892 (2014).
15. Plum, E., Fedotov, V. A. & Zheludev, N. I. Optical activity in extrinsically chiral metamaterial. *Appl. Phys. Lett.* **93**, 191911 (2008).
16. Plum, E. et al. Metamaterials: optical activity without chirality. *Phys. Rev. Lett.* **102**, 113902 (2009).
17. Barron, L. D. True and false chirality and absolute asymmetric synthesis. *J. Am. Chem. Soc.* **108**, 5539–5542 (1986).
18. Barron, L. D. True and false chirality and absolute enantioselection. *Rend. Lincei* **24**, 179–189 (2013).
19. Valev, V. K., Baumberg, J. J., Sibilia, C. & Verbiest, T. Chirality and chiroptical effects in plasmonic nanostructures: fundamentals, recent progress, and outlook. *Adv. Mater.* **25**, 2517–2534 (2013).
20. Hentschel, M., Schaferling, M., Duan, X., Giessen, H. & Liu, N. Chiral plasmonics. *Sci. Adv.* **3**, e1602735 (2017).
21. Mun, J. et al. Electromagnetic chirality: from fundamentals to nontraditional chiroptical phenomena. *Light Sci. Appl.* **9**, 139 (2020).
22. Hsu, C. W. et al. Observation of trapped light within the radiation continuum. *Nature* **499**, 188–191 (2013).
23. Hsu, C. W., Zhen, B., Stone, A. D., Joannopoulos, J. D. & Soljačić, M. Bound states in the continuum. *Nat. Rev. Mater.* **1**, 16048 (2016).
24. Koshelev, K., Lepeshov, S., Liu, M., Bogdanov, A. & Kivshar, Y. Asymmetric metasurfaces with high-Q resonances governed by bound states in the continuum. *Phys. Rev. Lett.* **121**, 193903 (2018).
25. Azzam, S. I., Shalaev, V. M., Boltasseva, A. & Kildishev, A. V. Formation of bound states in the continuum in hybrid plasmonic-photonic systems. *Phys. Rev. Lett.* **121**, 253901 (2018).
26. Liu, Z. et al. High-Q quasibound states in the continuum for nonlinear metasurfaces. *Phys. Rev. Lett.* **123**, 253901 (2019).
27. Yin, X., Jin, J., Soljacic, M., Peng, C. & Zhen, B. Observation of topologically enabled unidirectional guided resonances. *Nature* **580**, 467–471 (2020).
28. Poulikakos, L. V. et al. Optical chirality flux as a useful far-field probe of chiral near fields. *ACS Photonics* **3**, 1619–1625 (2016).
29. Cameron, R. P., Barnett, S. M. & Yao, A. M. Optical helicity, optical spin and related quantities in electromagnetic theory. *New J. Phys.* **14**, 053050 (2012).
30. Tang, Y. & Cohen, A. E. Enhanced enantioselectivity in excitation of chiral molecules by superchiral light. *Science* **332**, 333–336 (2011).
31. Taghizadeh, A. & Chung, I. S. Quasi bound states in the continuum with few unit cells of photonic crystal slab. *Appl. Phys. Lett.* **111**, 031114 (2017).
32. Hentschel, M. et al. Optical Properties of chiral three-dimensional plasmonic oligomers at the onset of charge-transfer plasmons. *ACS Nano* **6**, 10355–10365 (2012).
33. Zhang, S. et al. Photoinduced handedness switching in terahertz chiral metamolecules. *Nat. Commun.* **3**, 942 (2012).
34. Cui, Y., Kang, L., Lan, S., Rodrigues, S. & Cai, W. Giant chiral optical response from a twisted-arc metamaterial. *Nano Lett.* **14**, 1021–1025 (2014).
35. Chen, Y., Gao, J. & Yang, X. Chiral metamaterials of plasmonic slanted nanoapertures with symmetry breaking. *Nano Lett.* **18**, 520–527 (2018).
36. Wu, Z., Chen, X., Wang, M., Dong, J. & Zheng, Y. High-performance ultrathin active chiral metamaterials. *ACS Nano* **12**, 5030–5041 (2018).
37. Yang, S. et al. Spin-selective transmission in chiral folded metasurfaces. *Nano Lett.* **19**, 3432–3439 (2019).
38. Semnani, B., Flannery, J., Al Maruf, R. & Bajcsy, M. Spin-preserving chiral photonic crystal mirror. *Light Sci. Appl.* **9**, 23 (2020).
39. Zhu, A. Y. et al. Giant intrinsic chiro-optical activity in planar dielectric nanostructures. *Light Sci. Appl.* **7**, 17158 (2018).
40. Ji, C.-Y. et al. Artificial propeller chirality and counterintuitive reversal of circular dichroism in twisted meta-molecules. *Nano Lett.* **21**, 6828–6834 (2021).

Methods

Simulations

All the simulations in this work are conducted by a finite-element-method solver in COMSOL Multiphysics. Bloch boundary conditions are applied in the *x* and *y* directions, whereas perfectly matched layers are used in the *z* direction. The refractive index of the substrate and PMMA layer is set as 1.46, whereas the refractive index of TiO_2 is set as 2.13 + 0.001i.

Sample fabrication

A 220 nm TiO_2 is first deposited on the SiO_2 substrate by an electron beam evaporator (0.65 Å s^{-1}, Syskey Tech.) and then covered by a 20 nm Cr film (0.3 Å s^{-1}, Syskey Tech.) as a hard mask (Supplementary Fig. 5). Next, an 80 nm PMMA film is spin-coated and patterned by electron beam lithography. After the development of the resist, the pattern is transferred to the Cr film by an inductively coupled plasma (Oxford ICP180, gases: Cl_2 and O_2). Then, the whole sample is placed inside our home-made slant-etching system, and the gases of reactive ion etching we used are O_2, SF_6, Ar and CHF_3. Finally, the remaining Cr film is removed by a chromium etchant and a 400 nm PMMA film is spin-coated on the sample for index matching.

Optical characterization

A supercontinuum laser is used as the light source, and it is passed through a linear polarizer and a quarter-wave plate to generate circularly polarized light, which is then focused on the metasurface sample through an objective lens (Supplementary Fig. 7). The metasurface sample is positioned on a rotary stage so that the incident angle of the circularly polarized light can be controlled. The reflected and transmitted light are collected by the front and rear objective lenses, respectively. After passing through the quarter-wave plate and polarizer, their corresponding left-handed and right-handed circular components can be analysed.

Data availability

The data that support the plots within this paper and other findings of this study are available from the corresponding author upon reasonable request. The raw data can be accessed in the repository by the link: https://figshare.com/articles/dataset/Raw_Data_for_Nature_manuscript_2022-05-07139B/21257547.

Acknowledgements S.X. acknowledges support from the National Key Research and Development Project (grant no. 2021YFA1400802). Y.C. acknowledges support from the National Natural Science Foundation of China (No. 62275241) and the CAS Talents Programme. D.W. acknowledges support from the National Natural Science Foundation of China (grant no. 61927814). C.-W.Q. acknowledges financial support from the National Research Foundation, Prime Minister's Office, Singapore under the Competitive Research Programme Award NRF-CRP22-2019-0006. C.-W.Q. is also supported by a grant (no. R-261-518-004-720| A-0005947-16-00) from the Advanced Research and Technology Innovation Centre from the National University of Singapore.

Author contributions Y.C., S.X. and C.-W.Q. conceived the idea and designed the experiments. S.X. and C.-W.Q. supervised the project. Y.C. and W.C. conducted the simulations and theoretical analysis. H.D. and X.S. performed the experiments. Y.C., R.W., Y.-H.C., D.W., J.C., Y.S.K., S.X. and C.-W.Q analysed the data. Y.C. drafted the paper with inputs from all authors.

Competing interests The authors declare no competing interests.

Additional information
Supplementary information The online version contains supplementary material available at https://doi.org/10.1038/s41586-022-05467-6.
Correspondence and requests for materials should be addressed to Shumin Xiao or Cheng-Wei Qiu.
Peer review information *Nature* thanks the anonymous reviewers for their contribution to the peer review of this work.